

Landslides (2019) 16:23–35
 DOI 10.1007/s10346-018-1060-7
 Received: 7 March 2018
 Accepted: 5 September 2018
 Published online: 24 September 2018
 © Springer-Verlag GmbH Germany
 part of Springer Nature 2018

Alexander Roesner · Gauvain Wiemer · Stefan Kreiter · Stefan Wenau · Ting-Wei Wu ·
 Françoise Courboux · Volkhard Spiess · Achim Kopf

Impact of seismicity on Nice slope stability—Ligurian Basin, SE France: a geotechnical revisit

Abstract The shallow Nice submarine slope is notorious for the 1979 tsunamigenic landslide that caused eight casualties and severe infrastructural damage. Many previous studies have tackled the question whether earthquake shaking would lead to slope failure and a repetition of the deadly scenario in the region. The answers are controversial. In this study, we assess for the first time the factor of safety using peak ground accelerations (PGAs) from synthetic accelerograms from a simulated offshore Mw 6.3 earthquake at a distance of 25 km from the slope. Based on cone penetration tests (CPTu) and multichannel seismic reflection data, a coarser grained sediment layer was identified. In an innovative geotechnical approach based on uniform cyclic and arbitrary triaxial loading tests, we show that the sandy silt on the Nice submarine slope will fail under certain ground motion conditions. The uniform cyclic triaxial tests indicate that liquefaction failure is likely to occur in Nice slope sediments in the case of a Mw 6.3 earthquake 25 km away. A potential future submarine landslide could have a slide volume ($7.7 \times 10^6 \text{ m}^3$) similar to the 1979 event. Arbitrary loading tests reveal post-loading pore water pressure rise, which might explain post-earthquake slope failures observed in the field. This study shows that some of the earlier studies offshore Nice may have overestimated the slope stability because they underestimated potential PGAs on the shallow marine slope deposits.

Keywords Submarine landslides · Liquefaction · Earthquakes · Post-earthquake slope failure · Arbitrary triaxial loading · Nice

Introduction

The 1979 Airport Landslide offshore Nice is a well-examined submarine landslide example (Anthony and Julian 1997; Dan et al. 2007; Genesseeux et al. 1980; Sultan et al. 2004). The catastrophic failure on the Nice shallow submarine slope triggered a tsunami wave, which hit the coastline along the Ligurian Sea causing eight casualties and infrastructural damage (Dan et al. 2007; Migeon et al. 2006; Sahal and Lemahieu 2011). The interplay of land reclamation operations 6 months before the failure, extra loading by embankments of the extended Nice airport and heavy rainfall of 250 mm for 4 days before the failure most likely created an unstable artificial delta front slope, which collapsed on the 16 October 1979 (Anthony 2007; Anthony and Julian 1997; Dan et al. 2007; Kopf et al. 2016). Seismic loading did not trigger the 1979 failure; nevertheless, seismic loading is a prominent trigger for submarine landslides (Haque et al. 2016; Leynaud et al. 2017; Sultan et al. 2004), and the junction between the southern French-Italian Alps and the Ligurian Basin near Nice faces the highest seismicity in western Europe (Larroque et al. 2009; Salichon et al. 2010). Therefore, earthquake shaking needs to be considered as a potential trigger for future slope failures offshore Nice.

Granular loose sediments tend to contract under the cyclic loading imposed by earthquake shaking, which can transfer normal stress from the granular matrix onto the pore water if the soil is saturated and largely unable to drain during shaking. This eventually leads to zero normal effective stress and the sediment behaves as a liquid suspension; this process is called liquefaction (Idriss and Boulanger 2008; Ishihara 1985; Kramer 1996). The liquefaction potential is higher for loose than for dense granular sediments (Kramer 1996). In this context, the Nice slope sediment liquefaction potential is of special interest, because earthquake shaking may induce weakness in granular sediment layers and allow for the development of a shear plane of a submarine landslide (Sultan et al. 2004). In historical times, four devastating earthquakes, with intensities from 8 to 10 on the Mercalli scale and six more recent earthquakes since 1963, with magnitudes from 4 to 6, affected the Ligurian Basin (Migeon et al. 2006). Three historical tsunamis were generated by these earthquakes, damaging Ligurian Sea coastal infrastructure and causing casualties (Courboux et al. 2007; Ferrari 1991; Migeon et al. 2006). With approximately 2 million inhabitants and more than 5 million tourists every year, these events highlight the vulnerability of the densely populated Nice coastline, if a future tsunami were to strike the area.

Over the last two decades, several studies characterized the Nice submarine slope sediments and their stability via in situ measurements (Stegmann et al. 2011; Steiner et al. 2015; Sultan et al. 2010), laboratory experiments (Kopf et al. 2016; Stegmann and Kopf 2014; Sultan et al. 2004), high-resolution bathymetric data analysis (Kelner et al. 2016; Migeon et al. 2012), Envisat InSAR data (Cavalié et al. 2015), and numerical modeling (Dan et al. 2007; Steiner et al. 2015). These studies present contradictory results and interpretations concerning the Nice slope stability under earthquake ground motions. Sultan et al. (2004) compared cyclic triaxial tests to cyclic loads that may occur during earthquakes on the Nice slope with varying peak ground accelerations (PGAs) of 0.5, 1.0, and 1.5 m s^{-2} . They found that the cyclic loading caused by these PGAs were too low to initiate liquefaction failure in the tested sediment. They concluded that the liquefaction failure potential of Nice slope sediments is low due to a lack of loose sediment. In contrast, Dan et al. (2007) discussed that cyclic shaking may induce liquefaction in sand and silt interbeds present on the Nice slope. Ai et al. (2014) studied the cyclic stresses required for failure of the deeper continental slope offshore Nice and concluded that earthquakes with M 6.1–6.5 in an epicentral distance of < 15 km from the Nice slope are sufficient to initiate slope failure. The latest study in the Nice shallow submarine slope area by Kopf et al. (2016), however, stated that seismic loading is unlikely to be sufficient to trigger a major landslide unless an earthquake with a magnitude larger than the magnitudes of known historical events occurs.

Salichon et al. (2010) simulated realistic ground motions generated by a potential future Mw 6.3 earthquake that occurs on a reverse fault 25 km offshore Nice. They provided evidence for the occurrence of PGAs larger than any other geotechnical study in this region ever considered. The simulated accelerograms show median PGA values of up to 5.8 m s^{-2} . These values exceed those considered in the slope stability analysis by Sultan et al. (2004) by a factor of approximately four.

Based on these facts, we revisit the Nice shallow submarine slope area and investigate the seismic slope stability with cyclic triaxial tests with loading patterns and amplitudes based on the simulated accelerograms by Salichon et al. (2010). For this purpose, we used classic uniform cyclic triaxial and new arbitrary triaxial tests and compare them. The confining stress in the triaxial tests is based on cone penetration tests (CPTu) and seismic data interpretation.

Background

Geological setting

The Ligurian Basin was formed via rifting and seafloor spreading in the late Oligocene (Rehault et al. 1984; Savoye et al. 1993; Savoye and Piper 1991). It is a back-arc basin originating from the roll back of the Apennines-Maghrebides subduction zone. The offshore structure in the Ligurian Basin consists of a northern extensional margin with an east-northeast (ENE) trending graben, which is mainly related to southeast dipping faults. Nowadays,

the convergence rate between Africa and Eurasia is $4\text{--}5 \text{ mm a}^{-1}$ in $N 309 \pm 5^\circ$ direction (Nocquet 2012).

The Nice continental margin morphology is dominated by the Var river, a 135 km long river draining a 2820-km^2 area from the Alps towards the city of Nice (Fig. 1). The Var river transports $10 \text{ million m}^3 \text{ a}^{-1}$ of fine suspended sediments as well as $0.1 \text{ million m}^3 \text{ a}^{-1}$ of gravel (Dubar and Anthony 1995; Mulder et al. 1998). Most of the sediment is transported downslope into the submarine Var canyon. The coastline has a narrow continental shelf with a width of a hundred meters up to 2 km and a steep submarine slope with an average slope angle of 13° (Cochonat et al. 1993). The sediment builds a Gilbert-type fan delta at the river mouth (Dubar and Anthony 1995). Dubar and Anthony (1995) described the three upper major sedimentary delta facies with a thickness of approximately 120 m from bottom to top: (1) clast-supported gravel with a matrix of sand, (2) fine-grained shallow marine and estuarine/paludal deltaic sediments, and (3) fine-grained floodplain and paludal sediments with gravel channel deposits. Kopf et al. (2016) presented a more detailed facies analysis based on 72 cores where they described silt/sand interbeds as one out of three Pliocene-Holocene sediment facies. The silt/sand interbeds are of high interest for seismic slope stability because cohesionless sediment layers have a high liquefaction potential under cyclic loading (Boulanger and Idriss 2006; Idriss and Boulanger 2008; Kramer 1996). Based on eight CPTu (Fig. 1a), Sultan et al. (2010) showed that these coarse-grained layers are present at different depths, down to $\sim 30 \text{ mbsf}$ at the Nice slope.

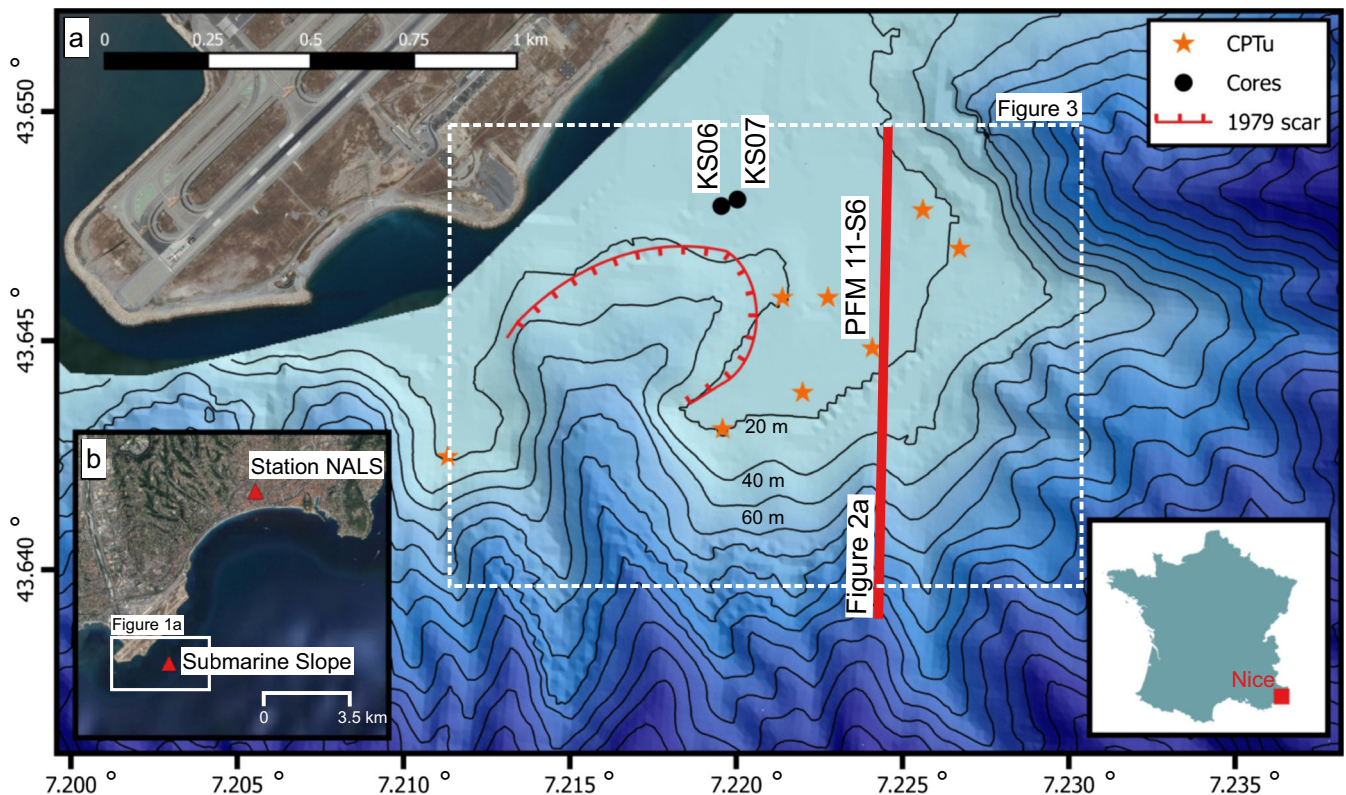


Fig. 1 a Map of the study area including the locations of Kullenberg cores KS06/07 and CPTu test. The red line indicates the seismic profile GeoB16-365 shown in Fig. 2a. The dashed box indicates the area presented in Fig. 3. b The inset shows the wider study area with the location of seismic station NALS. CPTu data and bathymetry were originally published by Sultan et al. (2010) and Dan et al. (2007)

Simulated ground motions

Ground motion simulations are often used to estimate accelerations of large earthquakes in regions with low seismicity, short recording history or when site effects are important. Salichon et al. (2010) used an empirical Green's function method developed by Kohrs-Sansorny et al. (2005) and widely applied since by several authors (Honoré et al. 2011; Wang et al. 2017). They simulated the ground motions that would be generated in the city of Nice by a Mw 6.3 earthquake occurring on a reverse fault 25 km offshore. This fault caused a Mw 4.5 earthquake in 2001 that was very well recorded by the permanent seismological network in the city of Nice (Couboulex et al. 2007). The fault is part of a fault network that extends from the Gulf of Genoa in Italy to Nice (Larroque et al. 2011). The eastern part of this fault has been identified as the nucleation of the large $M \sim 6.5$ – 6.8 earthquake that killed 600 people on the Ligurian coast in 1887 (Larroque et al. 2012). Salichon et al. (2010) used the recordings of the Mw 4.5 event in 2001 on eight stations as empirical Green's function in order to reproduce the site effects in the city of Nice. Indeed, significant site effects have been detected in some areas with amplification factors of up to 20 at frequencies of 1–2 Hz (Semblat et al. 2000). The approach uses three steps: (1) selection of the actual recordings of a smaller earthquake used as an empirical Green's function (here the Mw 4.5 event that occurred on February 25th 2001), (2) generation of a large number of source time functions that account for the possible variability of the rupture process of the modeled earthquake, and (3) convolution of both for each station. This approach created 500 simulated accelerograms for each station component. The NALS station (Fig. 1b) is of particular interest for our study because it is located on a 70-m-thick alluvial sediment deposit that is regarded as similar to the site conditions at the shallow submarine Nice slope. The median PGAs simulated for a Mw 6.3 earthquake are 5.8 m s^{-2} and 5.2 m s^{-2} for the NS and EW component, respectively. More details on the simulation of ground motion and related PGAs for the city of Nice are given in Salichon et al. (2010). Five modeled accelerograms out of the 500 at station NALS by Salichon et al. (2010) are of special interest for our study. These accelerograms represent the possible range of ground motion and are categorized according to their PGAs in minimum, 16th percentile, median, 84th percentile, and maximum (see also Table 2 in the appendix).

Material and methods

Sample material

In order to assess the shallow seismic slope stability offshore Nice, we performed earthquake simulating cyclic triaxial experiments on samples cored during the STEP 5 cruise in 2015 on the Nice shallow submarine slope (Thomas and Apprioual 2015). We took two Kullenberg cores KSo6 and KSo7, with respective lengths of 3.81 m and 4.25 m adjacent to the 1979 slide scar (Fig. 1a). The cored sediment consists of a few silty sediment layers interbedded within predominately clayey sediment similar to the sediment described by Kopf et al. (2016). Hereafter, the cored silty sediment layers are named sandy silt (Shepard 1954) or coarse-grained throughout the manuscript to emphasize that these layers constitute cohesionless and the coarsest sediment, thereby most prone to liquefaction, layers. These granular sediment layers are approximately 3–20 cm thick and are of special interest for the

liquefaction analysis. Since no silt or sand interbeds from 10 to 25 mbsf are available, we chose to use previously described coarse-grained interbeds from < 5 mbsf and consolidated them to confining stresses reigning at ~ 23 mbsf. This depth corresponds to the average depth of a prominent seismic reflector that correlates to CPTU profiles indicating coarse-grained sediments (Fig. 2).

Geotechnical testing

The sample material was geotechnically characterized by the grain size distributions, the Atterberg limits, and the parameters of the Mohr-Coulomb failure criterion. Grain size distributions of the coarse-grained sediments were measured via laser diffraction analysis with a Coulter LS-13320 (see Agrawal et al. 1991; Loizeau et al. 1994). We determined the Atterberg limits using the fall cone method (BS 1377-2:1990 1990; Kodikara et al. 2006) and the Mohr-Coulomb parameters using direct shear tests. The drained direct shear test samples were 56 mm in diameter and ~ 25 mm in height. The direct shear tests were performed in accordance with the German Institute for Standardization (DIN 18137-3 2002). The applied effective normal stress σ'_n ranged from 100 to 700 kPa and the shear displacement for each experiment was at least 12 mm. Effective normal stress, shear stress, as well as vertical and horizontal displacement were recorded at a frequency of 0.1 Hz. Shear rates were set to 0.02 mm min^{-1} which is considered sufficiently slow to allow constant drainage and complete pore water pressure dissipation (DIN 18137-3 2002). The Mohr-Coulomb failure criterion is defined as:

$$\tau = c' + \sigma'_n \tan \phi' \quad (1)$$

where c' is the effective cohesion, i.e., the extrapolated intercept of the Mohr-Coulomb envelope with the y -axis, ϕ' the effective angle of internal friction and τ the shear strength.

Liquefaction evaluation based on cyclic triaxial testing

Geotechnical liquefaction evaluation compares the seismic demand of expected earthquakes to the sediment cyclic resistance from laboratory experiments. Undrained cyclic shear tests determine the sediment response to earthquake shaking under defined stress boundary conditions, with pore water pressure evolution and sediment deformation as primary output information. Element tests are conducted under undrained conditions to simulate essentially undrained field conditions during earthquake loading. These tests are the standard procedure for liquefaction assessment, since they test the material behavior under a defined uniform stress state. The drainage state of a sediment in nature depends on the duration of the cyclic loading, the volume of the vulnerable sediment, its permeability, and the permeability of the surrounding sediment. The loading during an earthquake is fast, the tested sandy silt is not very permeable, and the surrounding finer grained sediments are even less permeable, that is why the in situ behavior is considered undrained even if the layer is not very thick. Earthquake shaking of Nice coarse-grained sediments was simulated via undrained cyclic shear strength experiments using the dynamic triaxial testing device (DTTD) (Wierner and Kopf 2017). The DTTD allows a wide range of testing configuration with its pressure compensated internal force sensor; further, details can be found in Kreiter et al. (2010). In this study, we applied

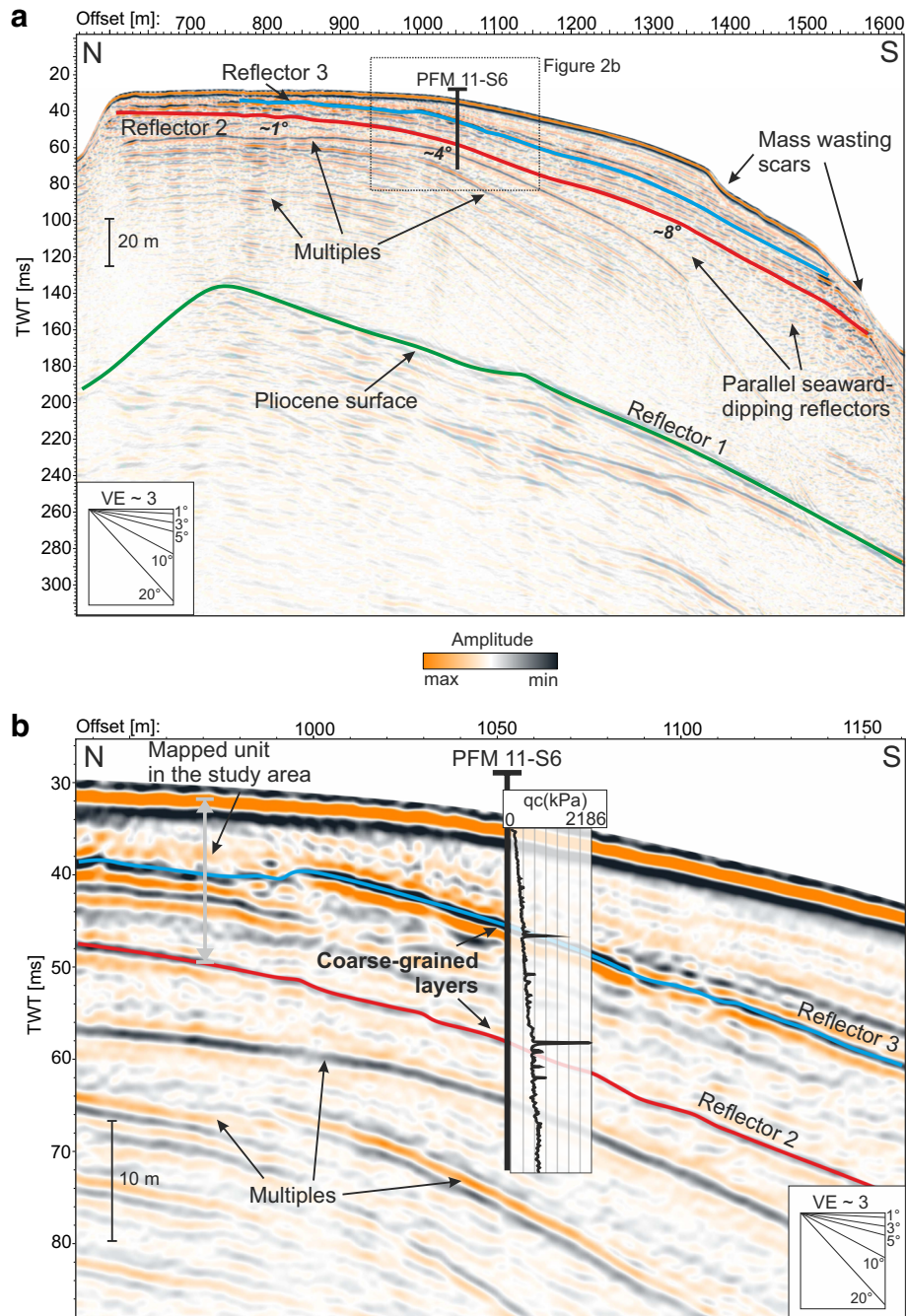


Fig. 2 a Multichannel seismic line GeoB16-365 shows the sedimentary succession of the Nice shelf. b Zoom in on seismic line GeoB16-365 with a scaled projection of CPTu measurement PFM 11-S6. The mapped reflectors R2 and R3 correspond to cone resistance maxima, suggesting coarse-grained sediment. CPTu data were originally published by Sultan et al. (2010)

the simplified procedure after Seed and Idriss (1971) and a new arbitrary loading procedure to evaluate the liquefaction potential. The simplified procedure parameterizes an arbitrary earthquake-loading signal (accelerogram) to an equivalent uniform series of shear stress cycles. The amplitude of the uniform shear stress cycles is set to 65% peak amplitude of the arbitrary

earthquake-loading signal. The maximum cyclic shear stress at depth induced by an earthquake is estimated by:

$$\tau_{eq} = 0.65 \times \frac{a_{max}}{g} \times \sigma_{v,c} \times r_d \quad (2)$$

where a_{max} is the horizontal peak ground acceleration at ground surface, g is the acceleration of gravity, $\sigma_{v,c}$ is the total vertical stress at depth z (target depth = ~ 23 mbsf), and r_d is the stress reduction factor. The stress reduction factor accounts for the damping of the soil as an elastic body (Seed and Idriss 1971). Details regarding the input parameters and the stress reduction factor are given in the appendix. Here, we apply this method to five simulated accelerograms for the Mw 6.3 earthquake described by Salichon et al. (2010) representing the full range of ground motions at station NALS. The stress of the seismic demand on a soil layer is often expressed as the cyclic shear stress ratio:

$$CSR_{eq} = \frac{\tau_{eq}}{\sigma'_{v,c}} \quad (3)$$

where τ_{eq} is normalized by the total vertical effective stress $\sigma'_{v,c}$ at depth z .

Amplitude and equivalent number of uniform loading cycles constitute the cyclic demand of an earthquake to the sediment at depth. Liu et al. (2001) developed an empirical regression function that evaluates the number of equivalent uniform stress cycles as a function of magnitude, site conditions, i.e., soil site or rock site, and the site-source distance. From our Mw 6.3 earthquake striking a soil site from a distance of 25 km, we derive 12 equivalent uniform stress cycles.

Eight undrained cyclic triaxial experiments were performed on (i) coarse-grained reconstituted and (ii) coarse-grained carefully handled natural, undisturbed core samples from the cores KSo6 and KSo7. These tests split up in six uniform cyclic triaxial tests and two arbitrary triaxial tests (Table 1). We accomplished the uniform cyclic triaxial tests on five reconstituted samples and one core sample. The uniform test on the core sample was performed in order to investigate the influence of the structural effect on the cyclic shear strength. All samples had a diameter of 3.5 cm and a height of approximately 7.4 cm. The samples were isotropically consolidated to a mean consolidation stress of 570 kPa including 400 kPa back-pressure sufficient to reach full sample saturation. Consequently, the mean effective consolidation stress p'_c is

170 kPa. Further details regarding sample preparation and consolidation can be found in the appendix. Uniform cyclic loading was applied at a frequency of 1 Hz. The cyclic loading is expressed with the triaxial cyclic shear stress ratio:

$$CSR_{cyc} = \frac{q_{cyc}}{2 \times \sigma'_{3c}} \quad (4)$$

$$q_{cyc} = \sigma'_1 - \sigma'_{3c} \quad (5)$$

where the single amplitude cyclic deviator stress q_{cyc} is calculated from the major principal effective stress σ'_1 and the minor principal effective consolidation stress σ'_{3c} . The CSR_{cyc} required for liquefaction in a specific number of loading cycles is also called soil cyclic resistance ratio (CRR). The excess pore water pressure Δu is expressed as excess pore pressure ratio:

$$r_u = \frac{\Delta u}{\sigma'_{3c}} \quad (6)$$

The number of cycles at failure were determined with the onset of liquefaction with $r_u = 1$.

The ratio of CRR and CSR_{eq} defines the factor of safety FS against liquefaction:

$$FS = \frac{CRR}{CSR_{eq}} \quad (7)$$

$FS > 1$ indicates a stable slope, whereas $FS < 1$ indicates slope failure.

The DTTD is well suited to load a sample with an arbitrary loading function (Kreiter et al. 2010). Hence, we skip all simplifications and load the sediment with a shear stress time series converted from a simulated accelerogram. We used a modified

Table 1 Triaxial test summary. The ID U1–6 are uniform cyclic and ID A1–2 arbitrary triaxial test. The abbreviation rec. stands for reconstituted sample

ID	Sample	Type	Water content	p'_c [kPa]	$CSR_{cyc}^a = CRR$	$CRR_{0.9}^b$	Void ratio	# of failure cycles
U1	KSo7_337cm	rec.	0.21	170	0.154	0.139	0.67	918
U2	KSo7_337cm	rec.	0.24	170	0.180	0.162	0.79	27
U3	KSo7_337cm	rec.	0.21	170	0.205	0.185	0.71	9
U4	KSo7_337cm	rec.	0.23	170	0.233	0.210	0.74	8
U5	KSo7_337cm	rec.	0.23	170	0.256	0.230	0.71	5
U6	KSo6_348cm	core	0.29	170	0.253	0.228	0.96	5
A1	KSo7_337cm	core	0.33	170	minimum modeled PGA	minimum modeled PGA	1.02	stable
A2	KSo7_337cm	core	0.29	170	16th percentile PGA	16th percentile PGA	0.96	failed

^a At failure

^b 90% of CRR, correction for unidirectional loading (appendix eq. (12))

version of eq. (2) to convert the provided minimum and 16th percentile accelerograms (in terms of PGA) to irregular shear stress histories:

$$\tau_{eq}(t) = \frac{a(t)}{g} \times \sigma_{v,c} \times r_d \quad (8)$$

where $a(t)$ is the horizontal ground acceleration over time at the ground surface, generated by the earthquake.

$$CSR_{eq}(t) = \frac{\tau_{eq}(t)}{\sigma'_{v,c}} \quad (9)$$

The $CSR_{eq}(t)$ is the irregular shear stress history normalized by the total vertical effective stress.

Multichannel seismic reflection data acquisition and processing

During the Poseidon cruise POS 500 in 2016, seismic data were acquired using the high-resolution multichannel seismic system from the Department of Geosciences of the University of Bremen (Kopf and Cruise Participants 2016). A Sercel Micro-GI-Gun with chamber volumes of 2×0.1 l yielding source frequencies of 80–400 Hz and a main frequency of 200 Hz, served as the seismic source. The acquisition system consisted of a 160-m-long Teledyne streamer with 64 channels. The seismic data has a vertical resolution of 2–4 m (Fig. 2). During post-processing, the data was common midpoint binned to 1 m, thus maximizing lateral resolution of the data. Fold of the data, i.e., the number of traces per bin, is usually 6–8. Furthermore, the data was bandpass-filtered, NMO-corrected using interactively picked velocity fields, CMP-stacked and migrated. For processing, the Vista Seismic Processing Software (Schlumberger) was used while interpretation was carried out in Kingdom (IHS). During interpretation, reflectors were

picked semi-automatically, gridded and isochore maps were calculated. Volumes were calculated for individual seismic units within a defined area.

Results

Slope geometry offshore Nice

The multichannel seismic reflection data shows the general reflection pattern of the Nice shelf area with gently seaward dipping strata (Fig. 2). Three horizons were picked, the lowermost Reflector 1 (R1) is the upper boundary of a set of low-frequency discontinuous reflector segments of medium amplitude that generally dip seaward (Fig. 2a). This surface is believed to be of Pliocene age and to consist of conglomerates (Auffret et al. 1982). Reflector 2 (R2) was mapped over most of the shelf area east of the 1979 landslide scar (Fig. 3). It is a medium amplitude continuous seaward-dipping reflector at a depth of less than 10 mbsf on the shelf and ~25 mbsf at the shelf edge. On the shelf, it lies almost horizontal while towards the shelf edge it dips seaward at $> 8^\circ$. At its seaward termination, it is truncated by the seafloor, indicating mass wasting scars at the upper slope. Between R1 and R2, only few reflectors are observed due to the presence of strong multiple reflections. However, the reflector pattern shows parallel to sub-parallel seaward-dipping reflectors below R2 at the shelf edge. Reflector 3 (R3) was mapped mostly on the outer shelf area (Fig. 2a) and is a continuous high amplitude reflector that terminates against the seafloor at its seaward termination as well as towards the shore. Its maximum depth lies, similarly to R2, on the outer shelf.

Both R2 and R3 correspond to layers of increased cone resistance in the CPTu profile PFM 11-S6 in Fig. 2b. Further, CPTu profiles are well correlated with the picked R2 and R3 reflectors (CPTu locations in Fig. 1a). While the high-amplitude R3

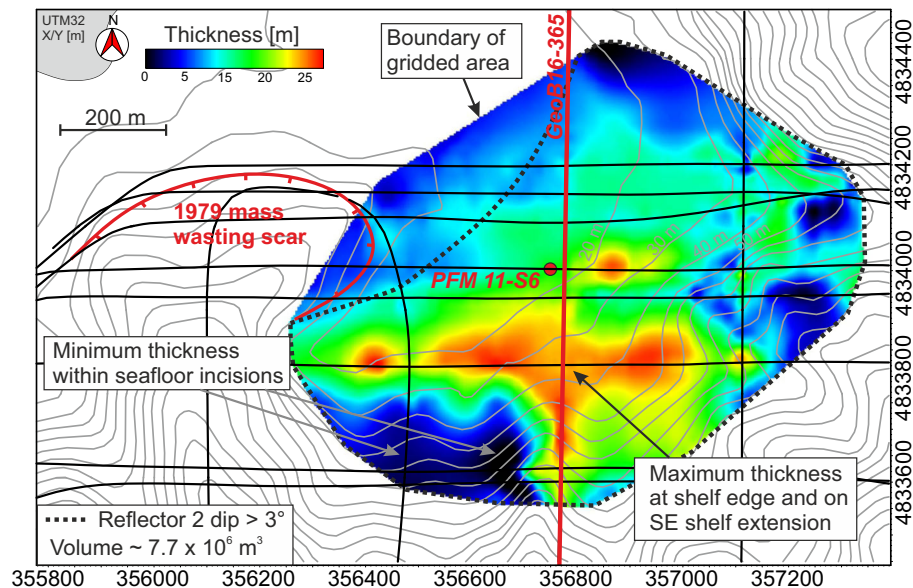


Fig. 3 Thickness map of the seismic unit between R2 and the seafloor. The gridding of horizons and thickness calculations were restricted to an area of interest on the shelf east of the 1979 mass wasting scar. Black lines indicate seismic profiles used for reflector mapping (see Fig. 2). Contour lines are calculated from the bathymetry shown in Fig. 1

corresponds to the second highest peak in the CPTu profile, the medium-amplitude R2 coincides with the overall maximum of the CPTu measurement.

The number of multichannel seismic profiles in the study area (Fig. 3) allowed us to map R2 on most of the shelf area. Figure 3 shows the thickness of the seismic unit between R2 and the seafloor, comprising most of the visible seaward-dipping shelf strata in our data. The picked horizon was gridded within the area of interest on the shelf east of the 1979 landslide scar. An isochore map was calculated using the picks of R2 and the seafloor which was subsequently time-depth converted using a velocity of 1600 m s^{-1} . The above-described profile GeoB16-365 is representative for the mapped unit. Hence, the thickness of the mapped unit varies between 0 and $\sim 25 \text{ mbsf}$ and its maximum thickness is located at the shelf edge while the thickness gradually decreases landwards (Fig. 3). At the upper slope, the unit thickness drops abruptly to zero in several places, usually coinciding with V-shaped seafloor incisions (Fig. 3). Kelner et al. (2016) analyzed these seafloor incisions in detail and described them as small landslide scars. The volume of the mapped unit was calculated in the area of interest where the dip of R2 exceeds 3° . We chose 3° as threshold value because this slope angle is typical for submarine landslide source areas (Hühnerbach and Masson 2004). The mapped volume comprises $\sim 7.7 \times 10^6 \text{ m}^3$. This volume lies in water depths between 20 and 80 m and focuses on the remnant shelf area towards the SE of the gridded area.

Geotechnical index properties and direct shear testing

The coarse-grained sediment layers in core KSo7 and KSo6 consist of clay, silt, and sand (Fig. 4). According to the Shepard classification scheme (Shepard 1954), all samples are silty sand or sandy silt. For our study, we regarded all samples as similar. We chose the sample KSo7_215cm with an intermediate grain size diameter at 50% cumulative grain size to derive index and mechanical parameters (inset in

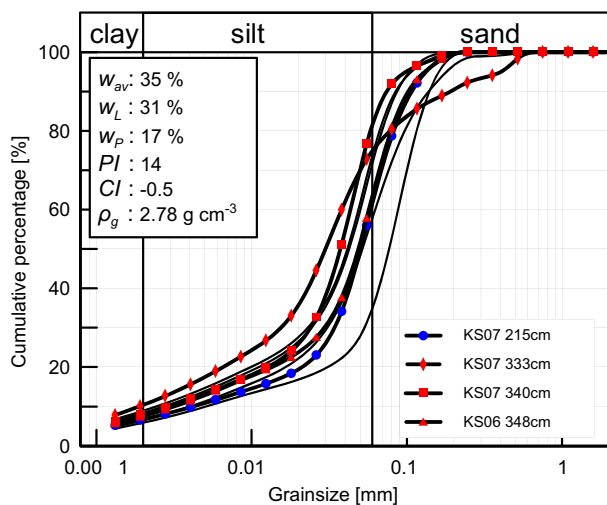


Fig. 4 Cumulative grain size distribution curves for KS06 and KS07 samples. Red squares/triangles/diamonds show triaxial test samples, whereas the blue dots represent direct shear test and Atterberg samples. w_{av} —average water content of sandy silt layers, w_L —liquid limit, w_P —plastic limit, PI —plasticity index, CI —consistency index, ρ_g —grain density

Fig. 4). The Atterberg limits show that our sediment is classified as low plastic clay with a liquid limit of 31% (inset in Fig. 4) (BS 5930:1999 + A2:2010 1999). The shear stress curves of the direct shear tests for initially loose sandy silt have not distinct peak and yield an effective critical angle of internal friction of 33° (Fig. 5a).

Uniform triaxial shear testing and factor of safety analysis

The test results of the uniform cyclic triaxial shear tests are presented as a function of loading cycles (Fig. 6a). Figure 6a exemplarily shows the evolution of the CSR_{cyc} , the pore pressure ratio r_u , and the axial strain with increasing number of loading cycles of a uniform cyclic triaxial test on a reconstituted sample sheared at a cyclic shear stress ratio CSR_{cyc} of 0.2. The pore pressure ratio increases with each loading cycle until it reaches unity and the sample is liquefied. The axial strain follows the typical pattern of cyclic triaxial tests on granular materials (Castro 1969). During the first four cycles, there is no significant strain. Only with increasing pore water pressure and hence decreasing effective stress, the sample deforms substantially. The primary outcome of such tests is the number of cycles a sample can bear at a given CSR_{cyc} (Table 1). The sample needs at small CSR_{cyc} a large number of cycles to failure, whereas large CSR_{cyc} cause failure in a few loading cycles. We evaluated the influence of structure and fabric of an undisturbed sample on cyclic shear strength by comparing a core sample with a reconstituted sample at the same CSR_{cyc} (Fig. 6b). Both samples show very similar pore water pressure and deformation response. Thus, the number of cycles to failure was the same in both tests, but the two samples had different void ratios (Table 1). The reconstituted and the core sample had a void ratio of 0.71 and 0.96, respectively.

The sediment cyclic strength curve based on the $CRR_{0.9}$ and number of cycles to failure is very well described by a power law function (Fig. 6b). This cyclic strength curve separates the plot into two areas: one above the line indicating unstable conditions and one below the line indicating stable conditions. A converted arbitrary loading signal that plots above the cyclic strength curve signifies that the earthquake-induced shear stresses are larger than the resistance of the samples and vice versa. All CSRs derived from the simulated accelerograms plot above the cyclic strength curve, in the unstable field. The median PGA of all 500 simulations conducted by Salichon et al. (2010) is shown by a square, whereas the range between the 16th and 84th percentiles representing $\sim 66\%$ of all 500 simulations. Hence, the factor of safety against liquefaction for all simulations is < 1 , which indicates sediment failure in the tested scenario. The Mw 6.3 earthquake with a median PGA results in a factor of safety of 0.58 and the minimum simulated PGA results in a factor of safety of 0.95. The seismic demand of a Mw 6.5 earthquake which Sultan et al. (2004) considered in their geotechnical analysis, plot in the stable field below the cyclic strength curve in Fig. 6b which is related to the consideration of lower PGA values than simulated by Salichon et al. (2010).

Arbitrary triaxial shear test

The CSR_{eq} , r_u , and axial strain of arbitrary loading tests are presented as a function of time in Fig. 7. Figure 7a shows the experimental results from the simulated accelerogram corresponding to the 16th percentile in terms of maximum shear stress (Fig. 6b) (Salichon et al. 2010). In general, the DTTD is able to respond to the requested earthquake input signal; however, during the major loading period in some cases, the response function reached only

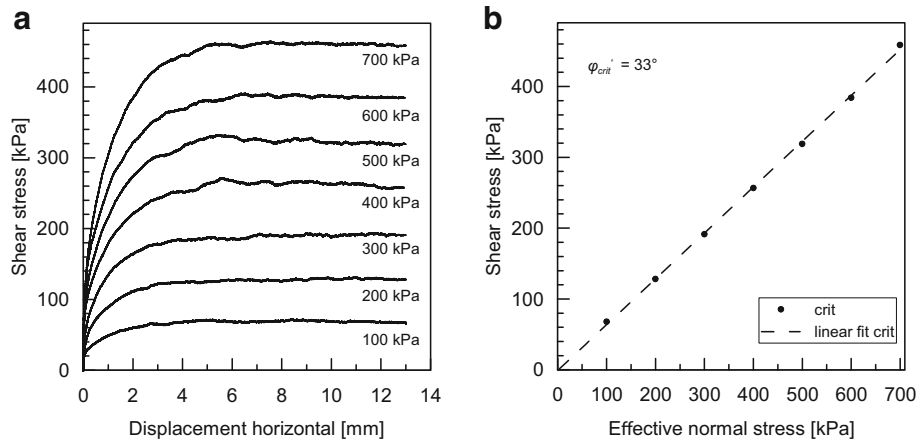


Fig. 5 a Direct shear test results of sample KS07_215cm. Numbers indicate normal stress. b Shear plane

up to 65% of the peak stress (inset in Fig. 7a). We measured a pore water pressure response immediately after loading starts; yet, we first detected a significant pore water pressure increase at a CSR_{eq} threshold of 0.1. The rapid increase of pore water pressure corresponds to the largest shear stresses induced by the largest accelerations. Significant deformation occurs simultaneously. The complete earthquake signal produced an excess pore pressure ratio of approximately 85%. However, an astonishing result is that the pore water pressure kept rising by 15% after the major loading pulse (10–18 s) had subsided. We reached initial liquefaction approximately 9 min after earthquake loading stopped. The second test (Fig. 7b) is based on the accelerogram with the minimum PGA out of 500 simulations (Salichon et al. 2010). Hence, it is comparable with the minimum CSR in Fig. 6b. In a few cases, the response function reached only up to 85% of the peak stress (inset in Fig. 7b). During loading, the pore pressure ratio increased to 30%. Simultaneously, the axial strain reaches 0.25%. Neither initial liquefaction nor significant axial strain occurred in this test.

During that test, we were not aware of the possible post-loading pore water pressure rise, which is why we stopped recording.

Discussion

Sample material and stress conditions

The geotechnical behavior of sandy silt is in general, not well understood, because its behavior is neither like a perfectly granular sediment as sand nor like cohesive sediment as clay. Many studies analyze cyclic behavior of either granular or cohesive sediments, but very little is known about the behavior of marine sandy silt deposits under cyclic loading. The sandy silt in this study shows characteristics of both granular sediment with $\phi'_{crit} = 33^\circ$ (Sadrekarimi and Olson 2011) and cohesive sediment by having Atterberg limits. Based on the index properties, the tested sediment cannot be characterized unambiguously as susceptible or non-susceptible to liquefaction. Whether or not a sediment type is susceptible to liquefaction may be estimated

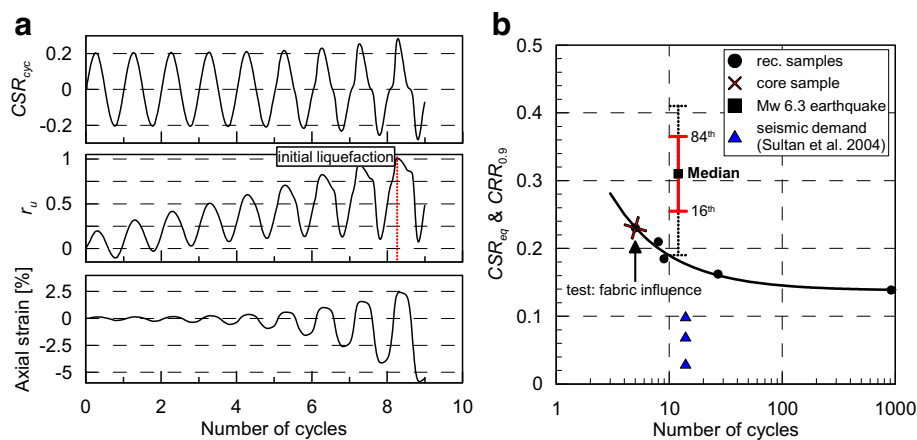


Fig. 6 a Undrained uniform cyclic triaxial test results of test U3. From top to bottom: uniform loading function, excess pore pressure ratio, and axial strain. Red dashed line indicates initial liquefaction. b CSR_{eq} and $CRR_{0.9}$ versus number of cycles to failure shows the cyclic strength curve and the CSR range of the modeled earthquake. The square indicates the CSR_{eq} derived from the median PGA published by Salichon et al. (2010), whereas the black dotted line presents the CSR range based on all 500 simulations and the red thick line present the 16th to 84th percentile of the 500 simulations. The blue triangles present the seismic demands of a Mw 6.5 earthquake used in the geotechnical study by Sultan et al. (2004)

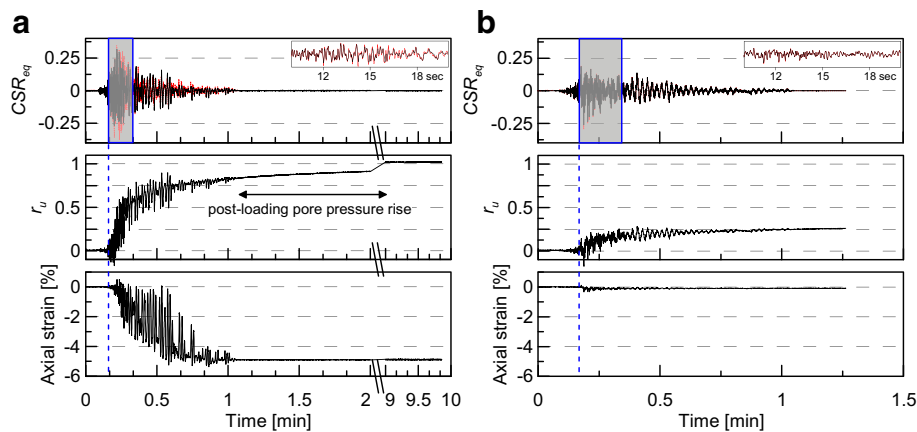


Fig. 7 **a** Undrained arbitrary triaxial test results of the 16th percentile modeled PGA earthquake. **b** Minimum modeled PGA earthquake. Top to bottom: input function (red dashed lines) and DTTD response function (black line); excess pore pressure ratio, axial strain. Y-axis scale of **a** and **b** are the same to illustrate differences between the tests. Insets show zoom of major loading period (shaded area). Blue dashed line illustrates CSR_{eq} threshold

from the Atterberg limits (Boulanger and Idriss 2006; Bray and Sancio 2006). After Boulanger and Idriss (2006), our samples are characterized as clay-like and non-susceptible to liquefaction. In contrast, after Bray and Sancio (2006), the samples of our study would be moderately susceptible. Our cyclic triaxial test results clearly document the liquefaction potential of the tested sediment and thereby highlight the necessity of such sophisticated testing procedures.

The effective normal stress in the triaxial tests was chosen based on CPTu and shallow water reflection seismic data. From the CPTu data, the high and medium amplitudes of R3 and R2 may be interpreted as coarse-grained sediments within the generally fine-grained clay-to-silt deposits of the study area (Kopf et al. 2016; Sultan et al. 2010). Both reflectors represent coarse-grained sediments in contrast to the surrounding sediment. Close to the shelf edge, R2 has an average depth of ~ 23 mbsf, which translates to 170 kPa vertical effective stress (appendix Table 2). Hence, in this study, we assume that coarse-grained sediment layers identified only as peaks in CPTu data and strong reflectors in seismic profiles are similar to coarse-grained sediments found in ~ 5 -m-long Kullenberg cores further upslope. This assumption can be made due to two facts: (1) the early to middle Holocene sedimentation pattern is characterized by a gap in gravel supply to the Var river mouth. Hence, silt and sand are the coarsest sediment supplied to the Var delta (Dubar and Anthony 1995). (2) This is confirmed by the longest core (17 m) MD01-2470 ever taken on the Nice submarine slope (Dan 2007). MD01-2470 shows sedimentary layers of clay and silty clay with recurring interbeds of silt and sometimes sand. Following seismic stratigraphy interpretation, these coarse-grained layers are seaward-dipping and are deepening with increasing distance from shore.

Huang et al. (2012) showed that cyclic resistance of the soil decreases with lower effective confining stress. Consequently, the granular layers in shallower depth, e.g., R3 or our cored sediments, would most likely liquefy under even smaller PGAs. By choosing a confining stress reigning at 23 mbsf, we present a worst-case scenario since a sudden failure nucleating at that depth is more likely to create a tsunami than a failure at 5 mbsf because of the larger slide volume.

It is well known that sample preparation affects the cyclic strength of sediments and that reconstituted samples are mostly less resistant than undisturbed samples (Idriss and Boulanger 2008; Mulilis et al. 1977). Structure and fabric are relevant for sediment strength. Remolding completely destroys the natural structure and fabric of a sediment sample. Yet, the reconstituted sample U5 and the core sample U6 failed after five cycles under identical loading amplitudes. Intuitively, we would expect the reconstituted sample to fail after fewer cycles than the core sample. However, the different void ratios of the samples may explain our results. The liquefaction resistance is closely linked to the void ratio of a sediment sample; the looser the sample the easier it is to liquefy (Kramer 1996). The core sample shows a higher void ratio than the reconstituted sample and is thus expected to be more prone to liquefaction. The similar measured liquefaction resistance of the reconstituted sample U5 and the mostly intact sample U6 may indicate that the looser state compensates the higher strength from intact fabric and structure. All cyclic uniform triaxial test samples after consolidation have a void ratio of 0.73 ± 0.06 , which is significantly lower than the void ratios of the three core samples of 0.99 ± 0.03 . The in situ void ratio in ~ 23 mbsf is unknown. However, the comparison of the core samples U6 and the reconstituted sample U5, both consolidated to the overburden stress reigning at ~ 23 mbsf, indicates that strength related to structure and fabric is compensated by lower void ratios in reconstituted samples. Hence, we tentatively assume that the cyclic strength curve ($R^2 = 0.96$) in Fig. 6b, which results from tests on reconstituted samples, is similar to a curve resulting from tests on undisturbed samples.

Nice seismogenic slope stability

The spatially widespread coarse-grained sediment layers are dipping seawards and are partly cut by some older slide scars. If a Mw 6.3 earthquake were to occur 25 km offshore, the sandy silt layers will liquefy and lose its entire shear strength. Since there is no backstop and since sediment has no tensile strength, a slope failure with a volume of $\sim 7.7 \times 10^6$ m³ would be the result. The volume is $\sim 11\%$ smaller than the initial 1979 slide volume calculated from differential bathymetry by Assier-Rzadkiewicz et al.

(2000) and ~23% smaller than the proposed volume by Labbé et al. (2012). Shallow water depth of 20–80 mbsl favors dangerous tsunamis (Harbitz et al. 2006). Labbé et al. (2012) and Assier-Rzadkiewicz et al. (2000) modeled the 1979 landslide as a flow of a viscous fluid with a medium viscosity. If the slide parameters regarding volume, slide geometry, viscosity, and water depth for a potential earthquake triggered submarine landslide would be similar, we speculate that a local tsunami comparable in size to the 1979 tsunami is possible even though the trigger mechanism of the two slides clearly differ.

The slope stability analysis presented in Sultan et al. (2004) is based on cyclic triaxial tests similar to the ones conducted in this study. The triaxial test results by Sultan et al. (2004) show a higher soil cyclic resistance compared to this study. However, the sample preparation, the sample dimensions, confining stresses, and void ratios of the samples are not documented. Furthermore, earthquake details such as, e.g., site-source distance, are missing. Thus, it is unfortunately not possible to compare our triaxial test results with those published by Sultan et al. (2004) in satisfactory detail. Moreover, the PGAs considered in their study are only approximately 25% of the median PGA (NALS) published by Salichon et al. (2010), which certainly means that these authors have not taken into account the site effects. Therefore, their results certainly overestimate the factor of safety. Our study considers an offshore Mw 6.3 earthquake causing high PGAs at station NALS within the city of Nice. At the time of the laboratory study, only data from the stations published in Salichon et al. (2010) were available, and therefore, station NALS was chosen as a reference station due to its proximity to the studied area and its geological setting. In October 2016, a new permanent broad band seismometer (PRIMA) has been installed offshore Nice on the shallow submarine slope at a depth of 17 mbsf. Data from the station is freely available through the RESIF Seismic data portal (<http://seismology.resif.fr/>). A first analysis of a few local earthquakes recorded at the station will be published soon by F. Courboux and colleagues. Based on this new data, we know that the ground motions recorded at station NALS are similar to the one at PRIMA station. Hence, our initial assumption is valid most likely because the site conditions are almost identical. Furthermore, the ground motions resulting from the rupture of the fault considered in Salichon et al. (2010) are not the only potential source for large PGAs at the shallow submarine Nice slope. A potential Mw 5.7 earthquake on the Blausasc fault north-east of Nice would also cause high PGAs ($> 1.5 \text{ m s}^{-2}$) in the city of Nice (Courboux et al. 2007) and may therefore also act as a trigger for a tsunamigenic submarine slope failure offshore Nice.

Liquefaction under arbitrary loading

First steps were taken to simulate arbitrary earthquake motions with the DTTD on core samples. The uniform tests indicate liquefaction for the full range of ground motions. In contrast, the arbitrary loaded test samples liquefied under 16th percentile acceleration in terms of all modeled PGAs but not under the minimum modeled PGA. However, the accumulated load of the earthquake input function is larger than the actual load subjected to the sample, because of limits of the DTTD (insets in Fig. 7). This discrepancy could explain the different results between uniform and arbitrary tests.

The ‘delayed liquefaction’ 9 min after loading with the 16th percentile PGA accelerogram is probably caused by localized liquefaction and slow seepage of the excess pore water pressure through relatively low permeable sediment to the sensor. Seepage is needed to transfer the pressure because of the compressibility of the sensor, the tubing and possibly some small air bubbles in the pores. The localization of the liquefaction may be caused by natural heterogeneity of the core sample, and localization in the central part is additionally promoted by the stabilization of the sample by friction at the sinter metal filters at the top and bottom of the sample. Other laboratory studies have directly measured localized pore water pressure rise in the shear zone (Thakur 2007).

Delayed pore water pressure rise or increased permeability in the field is probably the cause for landslides occurring minutes to days after earthquake loading at a quiet time without any tremor (Holzer et al. 1989; Ishihara 1984; Jibson et al. 1994). Post-earthquake pore water pressure rise was first observed at a field liquefaction experiment by Holzer et al. (1989); they explained the delay in pore water pressure rise by pore water pressure redistribution in the sediment. In natural slopes, it is probably the material heterogeneity and differences in loading which lead to localized pore water pressure rise, but to some extent is the ‘delayed liquefaction’ after the arbitrary triaxial loading test an analog to delayed failure after earthquake loading. Nevertheless, differences between arbitrary and uniform loading need further investigation and testing.

Conclusions

Several authors pointed out the likelihood of Mw ~6 earthquakes around the city of Nice (Courboux et al. 2007; Salichon et al. 2010). These earthquakes may generate large ground motions on alluvial Quaternary fillings, which may be much greater than those considered in earlier studies. Based on our study, we conclude that coarse-grained Quaternary sediment layers of the Var delta are prone to liquefaction during an Mw 6.3 earthquake produced 25 km offshore Nice. From uniform cyclic triaxial tests, we calculate a factor of safety against liquefaction < 1 for the Nice submarine slope sediments. Liquefied sediment may cause a slope failure similar in size to the 1979 event. Consequently, a local tsunami along the Nice coast is possible in the herein conceived scenario. The arbitrary tests are an innovative pilot study that leads to pore water pressure signals similar to observations made in the field. The observed post-loading pore water pressure rise is probably related to pore water pressure redistribution in the sample and is a potential slope failure triggering mechanism.

Acknowledgements

We thank our French colleagues from the “Institut français de recherche pour l’exploitation de la mer” for coring during their STEP 2015 oceanographic cruise DOI <https://doi.org/10.17600/15006100> on the research vessel L’Europe. Additionally, we thank the crew and scientists on board Poseidon cruise POS 500 for the seismic data acquisition. Moreover, we would like to thank Prof. Tobias Mörz for providing triaxial testing cells. Matthias Lange is thanked in memoriam for outstanding technical assistance with the DTTD. David Völker is thanked for fruitful discussions while working on this manuscript. We would like to thank Schlumberger

and IHS for providing academic licenses for Vista Seismic Processing Software and Kingdom respectively.

$$\tau_{cyc} = \frac{q_{cyc}}{2} \quad (11)$$

Funding information

This work was supported by the “Deutsche Forschungsgemeinschaft” via MARUM Research Center (Grants FZT15 and EXC309) in the area Seafloor Dynamics.

Appendix

Materials and methods

Cyclic Shear Stress

Any arbitrary earthquake signal can be translated into a uniform cyclic loading signal defined by a CSR_{eq} and an equivalent number of uniform cycles (Cetin and Seed 2004; Liu et al. 2001; Seed and Idriss 1971). The maximum cyclic shear stress was calculated at ~ 23 mbsf. The total vertical stress was calculated with an average bulk density of 1800 kg m^{-3} , which is representative for the slope sediments (Kopf and Cruise Participants 2008), and a Mediterranean water density of 1035 kg m^{-3} . The stress reduction factor accounts for the damping of the soil as an elastic body (Seed and Idriss 1971). Thus, it considers the variation of cyclic shear stresses with depth and was calculated according to a modified equation after Cetin and Seed (2004). The stress reduction factor is based on four descriptive variables:

$$r_d = \left(\frac{1 + \frac{-23.013 - 2.949 \times a_{max} + 0.999 \times M_w + 0.0525 \times V_{s12m}}{16.258 + 0.201 \times e^{0.341 \times (-20 + 0.0785 \times V_{s12m} + 7.586)}}}{1 + \frac{-23.013 - 2.949 \times a_{max} + 0.999 \times M_w + 0.0525 \times V_{s12m}}{16.258 + 0.201 \times e^{0.341 \times (0.0785 \times V_{s12m} + 7.586)}}} \right) - 0.0046 \times (d - 20) \quad (10)$$

where a_{max} is the peak ground acceleration, d is the depth of the sediment, V_{s12m} is the mean shear wave velocity in the upper 12 m of sediment, and M_w is the moment magnitude of the earthquake. Table 2 summarizes our input parameters to calculate the seismic demand (in terms of cyclic shear stress) at depth.

The cyclic shear stress is induced by cyclic vertical loading and unloading on a cylindrical sediment sample at constant lateral stress. The maximum cyclic shear stress τ_{cyc} in the triaxial sample is:

The samples were loaded in harmonic compression-extension mode (i.e., $q_{min} < 0 < q_{max}$ and $|q_{min}| = |q_{max}|$). The loading signal was applied with a frequency of 1 Hz. Both the loading pattern and the loading frequency are standards in earthquake engineering (ASTM Standard D5311/D5311M – 13 2013; Kramer 1996). The vertical displacement, principle stresses, deviator stress, and excess pore water pressure were recorded at 100 Hz during cyclic loading. Prior to each experiment, the samples were vacuum saturated to a Skempton B-value ≥ 0.92 (Skempton 1954) with deionized, deaerated water.

Seismic waves passing a sediment are associated with complex strain and stress paths near the ground surface, where the principle stresses change in direction and magnitude (El Shamy and Abdelhamid 2017). Thus, Seed et al. (1978) investigated the impact of multidirectional loading conditions and suggested a strength reduction factor of 10% for uniaxial loading. We corrected the CRR by 10% to account for the unidirectional loading during the triaxial tests.

$$CRR_{0.9} = CRR \times 0.9 \quad (12)$$

Sample Preparation

Most triaxial tests were conducted on reconstituted samples (of the original sediment) to make sure that (i) there are no mineralogical differences from one sample to another, (ii) the samples are homogenous, and (iii) we could perform as many tests as needed without running out of sample material. Reconstituted samples were prepared from a slurry following the approach from Bradshaw and Baxter (2007). The samples were prepared by mixing soil and water to a slurry with a water content of 33%, which is 2% higher than the liquid limit (Fig. 4). The slurry was filled in a cylindrical mold and tamped to remove air bubbles. The samples were one-dimensionally pre-consolidated to 100 kPa vertical stress. After pre-consolidation, the samples were set up in the triaxial cell and vacuum saturated for at least 2 h. In the DTTD, the samples were isotopically consolidated, with a ramp sufficient small to allow the sample to drain, to an effective confining stress of 170 kPa. This sample preparation procedure allowed us to create comparable homogenous samples with a small scatter in void ratios (Table 1):

Table 2 Input variables to calculate the seismic demand at a soil layer at ~ 23 mbsf for different PGAs of a modeled Mw 6.3 earthquake

Variable	Value	
a_{max}	3.1, 4.6, 5.8, 7.5, 12.1 m s^{-2} (minimum, 16th, median, 84th, maximum)	
g	9.81 m s^{-2}	
$\sigma_{v,c}$	~ 400 kPa	bulk density: 1800 kg m^{-3}
		depth: ~ 23 mbsf
$\sigma'_{v,c}$	~ 170 kPa	water density: 1035 kg m^{-3}
		depth: ~ 23 mbsf
r_d	0.40, 0.37, 0.35, 0.32, 0.22	V_{s12m} : 140 m s^{-1}
		depth: ~ 23 mbsf

$$e = \frac{V_V}{V_S} \quad (13)$$

where V_V is the volume of voids and V_S is the volume of solids.

In contrast, core samples were carefully extracted from the core via a metal cylinder to maintain the in situ fabric as good as possible. We used for core and reconstituted samples the same consolidation procedure. By comparing core and reconstituted samples under identical loading conditions, the influence of remolding on the cyclic shear strength was evaluated.

References

- Agrawal YC, McCave IN, Riley JB (1991) Laser diffraction size analysis. In: Svytski JPM (ed) Principles, methods, and application of particle size analysis. Cambridge University Press, Cambridge, pp 119–128
- Ai F, Förster A, Stegmann S, Kopf A (2014) Geotechnical characteristics and slope stability analysis on the deeper slope of the Ligurian margin, southern France. In: Sassa K (ed) Landslide science for a safer geoenvironment. Springer, Cham, pp 549–555
- Anthony EJ (2007) Problems of hazard perception on the steep, urbanised Var coastal floodplain and delta, French Riviera. *Méditerranée*:91–97. <https://doi.org/10.4000/mediterranee.180>
- Anthony EJ, Julian M (1997) The 1979 Var delta landslide on the French Riviera: a retrospective analysis. *J Coast Res* 13:27–35
- Assier-Rzadkiewicz S, Heinrich P, Sabatier PC, Savoye B, Bourillet JF (2000) Numerical modelling of a landslide-generated tsunami: the 1979 Nice event. *Pure Appl Geophys* 157:1707–1727. <https://doi.org/10.1007/PL00001057>
- ASTM Standard D5311/D5311M – 13 (2013) Test method for load controlled cyclic triaxial strength of soil
- Auffret GA, Auzende JM, Gennesseaux M, Monti S, Pastouret L, Pautot G, Vanney JR (1982) Recent mass wasting processes on the Provençal margin (western Mediterranean). In: Saxov S, Nieuwenhuis JK (eds) Marine slides and other mass movements. Springer, Boston, pp 53–58
- Boulanger RW, Idriss IM (2006) Liquefaction susceptibility criteria for silts and clays. *J Geotech Geoenviron* 132:1413–1426. [https://doi.org/10.1061/\(ASCE\)1090-0241\(2006\)132:11\(1413\)](https://doi.org/10.1061/(ASCE)1090-0241(2006)132:11(1413))
- Bradshaw AS, Baxter CDP (2007) Sample preparation of silts for liquefaction testing. *Geotech Test J* 30:324–332. <https://doi.org/10.1520/GTJ100206>
- Bray JD, Sancio RB (2006) Assessment of the liquefaction susceptibility of fine-grained soils. *J Geotech Geoenviron* 132:1165–1177. [https://doi.org/10.1061/\(ASCE\)1090-0241\(2006\)132:9\(1165\)](https://doi.org/10.1061/(ASCE)1090-0241(2006)132:9(1165))
- BS 1377–2:1990 (1990) Methods of test for soils for civil engineering purposes - part 2: classification tests. **British Standard Institution**, London
- BS 5930:1999+A2:2010 (1999) Code of practice for site investigations. **British Standard Institution**, London
- Castro G (1969) Liquefaction of sands: Dissertation. Harvard Soil Mechanics Series, vol 87. Harvard University, Cambridge, Massachusetts
- Cavalié O, Sladen A, Kelner M (2015) Detailed quantification of delta subsidence, compaction and interaction with man-made structures: the case of the NCA airport, France. *Nat Hazards Earth Syst Sci* 15:1973–1984. <https://doi.org/10.5194/nhess-15-1973-2015>
- Cetin OK, Seed RB (2004) Nonlinear shear mass participation factor (rd) for cyclic shear stress ratio evaluation. *Soil Dyn Earthq Eng* 24:103–113. <https://doi.org/10.1016/j.soildyn.2003.10.008>
- Cochonat P, Bourillet JF, Savoye B, Dodd L (1993) Geotechnical characteristics and instability of submarine slope sediments, the Nice slope (N-W Mediterranean Sea). *Mar Georesour Geotechnol* 11:131–151. <https://doi.org/10.1080/1064199309379912>
- Courboux F, Larroque C, Deschamps A, Kohrs-Sansorny C, Gélis C, Got JL, Charreau J, Stéphan JF, Béthoux N, Virieux J, Brunel D, Maron C, Duval AM, Perez J-L, Mondelli P (2007) Seismic hazard on the French Riviera: observations, interpretations and simulations. *Geophys J Int* 170:387–400. <https://doi.org/10.1111/j.1365-246X.2007.03456.x>
- Dan G (2007) Processus gravitaires et evaluation de la stabilité des pentes: Approches géologiques et géotechnique: Dissertation. University Bretagne occidentale, Brest
- Dan G, Sultan N, Savoye B (2007) The 1979 Nice harbour catastrophe revisited: trigger mechanism inferred from geotechnical measurements and numerical modelling. *Mar Geol* 245:40–64. <https://doi.org/10.1016/j.margeo.2007.06.011>
- DIN 18137-3 (2002) Baugrund, Untersuchung von Bodenproben - Bestimmung der Scherfestigkeit - Teil. Direkter Scherversuch. Deutsches Institut für Normung, Berlin, p 3
- Dubar M, Anthony EJ (1995) Holocene environmental change and river-mouth sedimentation in the Baie des Anges, French Riviera. *Quat Res* 43:329–343. <https://doi.org/10.1006/qres.1995.1039>
- El Shamy U, Abdelhamid Y (2017) Some aspects of the impact of multidirectional shaking on liquefaction of level and sloping granular deposits. *J Eng Mech* 143:C4016003–1–C4016003–17. [https://doi.org/10.1061/\(ASCE\)EM.1943-7889.0001049](https://doi.org/10.1061/(ASCE)EM.1943-7889.0001049)
- Ferrari G (1991) The 1887 Ligurian earthquake: a detailed study from contemporary scientific observations. *Tectonophysics* 193:131–139. [https://doi.org/10.1016/0040-1951\(91\)90194-W](https://doi.org/10.1016/0040-1951(91)90194-W)
- Gennesseaux M, Mauffret A, Pautot G (1980) Les glissements sous-marins de la pente continentale niçoise et la rupture de câbles en mer Ligure (Méditerranée occidentale). *Comptes Rendus de l'Académie des Sciences de Paris* 290(14):959–962
- Haque U, Blum P, da Silva PF, Andersen P, Pilz J, Chalov SR, Malet J-P, Auflič MJ, Andres N, Poyiadji E, Lamas PC, Zhang W, Peshevski I, Pétursson HG, Kurt T, Dobrev N, Garcia-Davallilo JC, Halkia M, Ferri S, Gaprindashvili G, Engström J, Keellings D (2016) Fatal landslides in Europe. *Landslides* 13:1545–1554. <https://doi.org/10.1007/s10346-016-0689-3>
- Harbitz CB, Løvholt F, Pedersen G, Masson DG (2006) Mechanisms of tsunami generation by submarine landslides: a short review. *Nor J Geol* 86:255–264
- Holzer TL, Hanks TC, Youd TL (1989) Dynamics of liquefaction during the 1987 Superstition Hills, California, earthquake. *Science* 244:56–59. <https://doi.org/10.1126/science.244.4900.56>
- Honoré L, Courboux F, Souriau A (2011) Ground motion simulations of a major historical earthquake (1660) in the French Pyrenees using recent moderate size earthquakes. *Geophys J Int* 187:1001–1018. <https://doi.org/10.1111/j.1365-246X.2011.05193.x>
- Huang Y, Zheng H, Zhuang Z (2012) Seismic liquefaction analysis of a reservoir dam foundation in the south–north water diversion project in China. Part I: liquefaction potential assessment. *Nat Hazards* 60:1299–1311. <https://doi.org/10.1007/s11069-011-9910-9>
- Hühnerbach V, Masson DG (2004) Landslides in the North Atlantic and its adjacent seas: an analysis of their morphology, setting and behaviour. *Mar Geol* 213:343–362. <https://doi.org/10.1016/j.margeo.2004.10.013>
- Idriss IM, Boulanger RW (2008) Soil liquefaction during earthquakes. Engineering monographs on miscellaneous earthquake engineering topics, MNO-12. Earthquake Engineering Research Institute, Berkeley
- Ishihara K (1984) Post-earthquake failure of a tailings dam due to liquefaction of pond deposit. **International Conference on Case Histories in Geotechnical Engineering**
- Ishihara K (1985) Stability of natural deposits during earthquakes: 11th International conference on soil mechanics and foundation engineering. Proceedings, San Francisco, pp 321–376
- Jibson RW, Prentice CS, Borisoff BA, Rogozhin EA, Langer CJ (1994) Some observations of landslides triggered by the 29 April 1991 Racha earthquake, republic of Georgia. *Bull Seismol Soc Am* 84:963–973
- Kelner M, Migeon S, Tric E, Courboux F, Dano A, Lebourg T, Taboada A (2016) Frequency and triggering of small-scale submarine landslides on decadal timescales: analysis of 4D bathymetric data from the continental slope offshore Nice (France). *Mar Geol* 379:281–297. <https://doi.org/10.1016/j.margeo.2016.06.009>
- Kodikara J, Seneviratne HN, Wijayakulasooriya CV (2006) Discussion of “using a small ring and a fall-cone to determine the plastic limit” by Tao-Wei Feng. *J Geotech Geoenviron* 132:276–278. [https://doi.org/10.1061/\(ASCE\)1090-0241\(2006\)132:2\(276\)](https://doi.org/10.1061/(ASCE)1090-0241(2006)132:2(276))
- Kohrs-Sansorny C, Courboux F, Bour M, Deschamps A (2005) A two-stage method for ground-motion simulation using stochastic summation of small earthquakes. *Bull Seismol Soc Am* 95:1387–1400. <https://doi.org/10.1785/0120040211>
- Kopf A, Cruise participants (2008) report and preliminary results of METEOR cruise M73/1: LIMA-LAMO (Ligurian margin landslide measurement & observatory), Cadiz 22.07.2007 – Genoa 11.08.2007. Berichte aus dem Fachbereich Geowissenschaften der Universität Bremen
- Kopf A, Cruise Participants (2016) Report and preliminary results of R/V POSEIDON cruise POS 500, LISA, Ligurian slope AUV mapping, gravity coring and seismic reflection, Catania (Italy) – Malaga (Spain), 25.05.2016–09.06.2016. Berichte aus dem Fachbereich Geowissenschaften der Universität Bremen
- Kopf A, Stegmann S, Garziglia S, Henry P, Dennielou B, Haas S, Weber K-C (2016) Soft sediment deformation in the shallow submarine slope off Nice (France) as a result of a variably charged Pliocene aquifer and mass wasting processes. *Sediment Geol* 344:290–309. <https://doi.org/10.1016/j.sedgeo.2016.05.014>
- Kramer SL (1996) Geotechnical earthquake engineering. Prentice-hall international series in civil engineering and engineering mechanics. Prentice Hall, Upper Saddle River, NJ

- Kreiter S, Moerz T, Strasser M, Lange M, Schunn W, Schlue BF, Otto D, Kopf A (2010) Advanced dynamic soil testing — introducing the new Marum dynamic triaxial testing device. In: Mosher DC, Shipp RC, Moscardelli L, Chaytor JD, Baxter CDP, Lee HJ, Urgeles R (eds) Submarine mass movements and their consequences: 4th international symposium. Springer, Dordrecht, pp 31–41
- Labbé M, Donnadiou C, Daubord C, Hébert H (2012) Refined numerical modeling of the 1979 tsunami in Nice (French Riviera): comparison with coastal data. *J Geophys Res* 117:1–17. <https://doi.org/10.1029/2011JF001964>
- Larroque C, Delouis B, Godel B, Nocquet J-M (2009) Active deformation at the south-western Alps–Ligurian basin junction (France–Italy boundary): evidence for recent change from compression to extension in the Argentera massif. *Tectonophysics* 467:22–34. <https://doi.org/10.1016/j.tecto.2008.12.013>
- Larroque C, Lépinay d, Mercier B, Migeon S (2011) Morphotectonic and fault–earthquake relationships along the northern Ligurian margin (western Mediterranean) based on high resolution, multibeam bathymetry and multichannel seismic-reflection profiles. *Mar Geophys Res* 32:163–179. <https://doi.org/10.1007/s11001-010-9108-7>
- Larroque C, Scotti O, Ioualalen M (2012) Reappraisal of the 1887 Ligurian earthquake (western Mediterranean) from macroseismicity, active tectonics and tsunami modeling. *Geophys J Int* 190:87–104. <https://doi.org/10.1111/j.1365-246X.2012.05498.x>
- Leynaud D, Mulder T, Hanquiez V, Gonthier E, Régert A (2017) Sediment failure types, preconditions and triggering factors in the Gulf of Cadiz. *Landslides* 14:233–248. <https://doi.org/10.1007/s10346-015-0674-2>
- Liu AH, Stewart JP, Abrahamson NA, Moriwaki Y (2001) Equivalent number of uniform stress cycles for soil liquefaction analysis. *J Geotech Geoenviron* 127:1017–1026. [https://doi.org/10.1061/\(ASCE\)1090-0241\(2001\)127:12\(1017\)](https://doi.org/10.1061/(ASCE)1090-0241(2001)127:12(1017))
- Loizeau J-L, Arbouille D, Santiago S, Vernet J-P (1994) Evaluation of a wide range laser diffraction grain size analyser for use with sediments. *Sedimentology* 41:353–361. <https://doi.org/10.1111/j.1365-3091.1994.tb01410.x>
- Migeon S, Mulder T, Savoye B, Sage F (2006) The Var turbidite system (Ligurian Sea, northwestern Mediterranean)—morphology, sediment supply, construction of turbidite levee and sediment waves: implications for hydrocarbon reservoirs. *Geo-Mar Lett* 26:361–371. <https://doi.org/10.1007/s00367-006-0047-x>
- Migeon S, Cattaneo A, Hassoun V, Dano A, Casadevant A, Ruellan E (2012) Failure processes and gravity-flow transformation revealed by high-resolution AUV swath bathymetry on the Nice continental slope (Ligurian Sea). In: Yamada Y, Kawamura K, Ikehara K, Ogawa Y, Urgeles R, Mosher D, Chaytor J, Strasser M (eds) Submarine mass movements and their consequences: 5th international symposium. Springer, Dordrecht, pp 451–461
- Mulder T, Savoye B, Piper DJW, Syvitski JPM (1998) The Var submarine sedimentary system: understanding Holocene sediment delivery processes and their importance to the geological record. *Geol Soc Lond, Spec Publ* 129:145–166. <https://doi.org/10.1144/GSL.SP.1998.129.01.10>
- Mullis JP, Arulanandan K, Mitchell JK, Chan CK, Seed HB (1977) Effects of sample preparation on sand liquefaction. *J Geotech Eng Div* 103:91–108
- Nocquet J-M (2012) Present-day kinematics of the Mediterranean: a comprehensive overview of GPS results. *Tectonophysics* 579:220–242. <https://doi.org/10.1016/j.tecto.2012.03.037>
- Rehault J-P, Boillot G, Mauffret A (1984) The western Mediterranean basin geological evolution. *Mar Geol* 55:447–477. [https://doi.org/10.1016/0025-3227\(84\)90081-1](https://doi.org/10.1016/0025-3227(84)90081-1)
- Sadrekarimi A, Olson SM (2011) Critical state friction angle of sands. *Géotechnique* 61:771–783. <https://doi.org/10.1680/geot.9.P.090>
- Sahal A, Lemahieu A (2011) The 1979 Nice airport tsunami: mapping of the flood in Antibes. *Nat Hazards* 56:833–840. <https://doi.org/10.1007/s11069-010-9594-6>
- Salichon J, Kohrs-Sansorny C, Bertrand E, Courboux F (2010) A mw 6.3 earthquake scenario in the city of Nice (Southeast France): ground motion simulations. *J Seismol* 14:523–541. <https://doi.org/10.1007/s10950-009-9180-0>
- Savoye B, Piper DJW (1991) The Messinian event on the margin of the Mediterranean Sea in the Nice area, southern France. *Mar Geol* 97:279–304. [https://doi.org/10.1016/0025-3227\(91\)90121-J](https://doi.org/10.1016/0025-3227(91)90121-J)
- Savoye B, Piper DJW, Droz L (1993) Plio-Pleistocene evolution of the Var deep-sea fan off the French Riviera. *Mar Pet Geol* 10:550–560. [https://doi.org/10.1016/0264-8172\(93\)90059-2](https://doi.org/10.1016/0264-8172(93)90059-2)
- Seed BH, Idriss I (1971) Simplified procedure for evaluating soil liquefaction potential. *J Soil Mech Found Div* 97:1249–1273
- Seed BH, Pyke RM, Martin GR (1978) Effect of multidirectional shaking on pore pressure development in sands. *J Geotech Eng Div* 104:27–44
- Semblat J-F, Duval A-M, Dangla P (2000) Numerical analysis of seismic wave amplification in Nice (France) and comparisons with experiments. *Soil Dyn Earthq Eng* 19:347–362. [https://doi.org/10.1016/S0267-7261\(00\)00016-6](https://doi.org/10.1016/S0267-7261(00)00016-6)
- Shepard FP (1954) Nomenclature based on sand-silt-clay ratios. *J Sediment Res* 24:151–158. <https://doi.org/10.1306/D4269774-2B26-11D7-8648000102C1865D>
- Skempton AW (1954) The pore-pressure coefficients a and b . *Géotechnique* 4:143–147. <https://doi.org/10.1680/geot.1954.4.4.143>
- Stegmann S, Kopf A (2014) How stable is the Nice slope? – an analysis based on strength and cohesion from ring shear experiments. In: Krastel S, Behrmann J-H, Völker D, Stipp M, Berndt C, Urgeles R, Chaytor J, Huhn K, Strasser M, Harbitz CB (eds) Submarine mass movements and their consequences: 6th international symposium. Springer, Cham, pp 189–199
- Stegmann S, Sultan N, Kopf A, Apprioual R, Pelleau P (2011) Hydrogeology and its effect on slope stability along the coastal aquifer of Nice, France. *Mar Geol* 280:168–181. <https://doi.org/10.1016/j.margeo.2010.12.009>
- Steiner A, Kopf A, Henry P, Stegmann S, Apprioual R, Pelleau P (2015) Cone penetration testing to assess slope stability in the 1979 Nice landslide area (Ligurian margin, SE France). *Mar Geol* 369:162–181. <https://doi.org/10.1016/j.margeo.2015.08.008>
- Sultan N, Cochonat P, Canals M, Cattaneo A, Dennielou B, Hafidason H, Laberg JS, Long D, Mienert J, Trincardi F, Urgeles R, Vorren TO, Wilson C (2004) Triggering mechanisms of slope instability processes and sediment failures on continental margins: a geotechnical approach. *Mar Geol* 213:291–321. <https://doi.org/10.1016/j.margeo.2004.10.011>
- Sultan N, Savoye B, Jouet G, Leynaud D, Cochonat P, Henry P, Stegmann S, Kopf A (2010) Investigation of a possible submarine landslide at the Var delta front (Nice continental slope, Southeast France). *Can Geotech J* 47:486–496. <https://doi.org/10.1139/T09-105>
- Thomas Y, Apprioual R (2015) STEP 2015 cruise, L'Europe R/V. doi: <https://doi.org/10.17600/15006100>
- Wang H, Wen R, Ren Y (2017) Simulating ground-motion directivity using stochastic empirical Green's function method. *Bull Seismol Soc Am* 107:359–371. <https://doi.org/10.1785/0120160083>
- Wiemer G, Kopf A (2017) On the role of volcanic ash deposits as preferential submarine slope failure planes. *Landslides* 14:223–232. <https://doi.org/10.1007/s10346-016-0706-6>

A. Roesner (✉) · G. Wiemer · S. Kreiter · S. Wenau · T.-W. Wu · V. Spiess · A. Kopf

MARUM – Center for Marine Environmental Sciences, University of Bremen, Bremen, Germany
Email: aroesner@uni-bremen.de

S. Wenau · V. Spiess
Faculty of Geosciences, University of Bremen, Bremen, Germany

F. Courboux
Université Côte d'Azur CNRS, IRD, Observatoire de la Côte d'Azur, Géoazur, Valbonne, France